Pure Appl. Chem., Vol. 75, No. 7, pp. 889–903, 2003.
© 2003 IUPAC

Materials in thermodynamic potential gradients*

M. Martin‡

Institute of Physical Chemistry, Aachen University of Technology, Templergraben 59, D-52056 Aachen, Germany

Abstract: In materials that are exposed to thermodynamic potential gradients (i.e., gradients of chemical potentials, electrical potential, temperature, or pressure), transport processes of the mobile components occur. These transport processes and the coupling between different processes are not only of fundamental interest, but are also the origin of degradation processes, such as kinetic demixing and decomposition and changes in the morphology of the material, all of which are of great practical relevance. Two classes of materials will be considered: semi- and ion-conducting oxides and ion-conducting halides. In oxides, kinetic demixing of the cations in a multicomponent oxide and kinetic decomposition of the oxide under the influence of an applied thermodynamic potential gradient will be considered for homovalent oxide solid solutions and for heterovalently doped oxides. In ion-conducting halides, the morphological stability of solid/solid interfaces, which are driven by an external electrical potential gradient, is studied. Monte Carlo simulations show that the morphological stability of the interface is determined by the difference in the ionic conductivities of the two crystals.

INTRODUCTION

In many applications, originally homogeneous materials are exposed to a thermodynamic potential gradient, which can be a gradient of temperature, chemical potential of one or more elements, electrical potential, or uniaxial pressure. Some well-known examples are tarnishing layers on metallic materials [1,2], which act as corrosion protection, thermal barrier coatings [3] acting as heat shield, solid electrolytes in fuel cells [4], or gas-separation membranes [5]. The applied gradients act as a generalized thermodynamic force and induce directed fluxes of the mobile components. These fluxes may lead to three basic degradation phenomena of the materials.

- The multicomponent material, which was originally chemically homogeneous, becomes chemically inhomogeneous (so-called kinetic demixing).
- Formation of new phases might take place, i.e., the initially single-phase material might decompose into new phases (so-called kinetic decomposition).
- The original morphology of the material might become unstable and a new morphology might be established (morphological instability).

It must be emphasized that all three phenomena have a purely kinetic origin, i.e., if the applied thermodynamic potential gradient is removed, the directed fluxes will disappear, and owing to diffusion processes the material will again become homogeneous, the new phases will disappear, and the new morphology might become unstable and the old one might be reestablished.

---

*Plenary lecture presented at the 17th IUPAC Conference on Chemical Thermodynamics (ICCT), Rostock, Germany, 28 July–2 August 2002. Other presentations are published in this issue, pp. 859–936.

‡E-mail: martin@rwth-aachen.de

In this article, some theoretical considerations will be made on the thermodynamics and kinetics of the above degradation processes, experimental results with model systems will be reported, and implications for applications of materials in thermodynamic potential gradients will be discussed.

The class of materials will be limited to oxides and halides. Owing to their physical properties, oxides are used in many technical applications, which have been discussed above. Examples are Al_2O_3 tarnishing layers on metallic alloys [1], ZrO_2 layers in thermal barrier coatings [3], Y_2O_3-doped ZrO_2 (YSZ) being the solid electrolyte and (La,Sr)$MnO_{3-\delta}$ being the cathode material in solid oxide fuel cells (SOFC) [4], or (La,Sr)$CrO_{3-\delta}$ in oxygen-separation membranes [5]. Halides, on the other hand, are well-studied materials with precisely known properties that can be used as simple model systems in experiments [6].

KINETIC DEMIXING

Demixing of oxides in an oxygen potential gradient

At first, we will consider only oxides where the oxygen ions are practically immobile* and which are good semiconductors (e.g., simple transition-metal oxides such as CoO, NiO, or MnO). For the sake of simplicity, we will treat only binary oxides, $(A_{1-x}B_x)O$**. These oxides have four thermodynamic degrees of freedom, which are the pressure, p, the temperature, T, the composition, x, and the chemical potential of oxygen, $\mu_{O_2} = \mu^0_{O_2} + RT\ln(p_{O_2}/p^0$ (p_{O_2} is the oxygen partial pressure and $p^0 = 1$ bar the standard pressure). If such an oxide is exposed to an oxygen potential gradient (without any gradient in total pressure, p, or temperature, T), gradients of the chemical potentials of the chemical components A and B are induced as a consequence of the Gibbs–Duhem relation, $x_A d\mu_A + x_B d\mu_B + x_O d\mu_O = 0$ (see Fig. 1a). These thermodynamic forces generate fluxes of the mobile components, which are the cations, A^{2+} and B^{2+}, and electronic defects, e.g., electron holes, $h^\bullet$, in a p-type semiconductor. The cations are assumed to be mobile by means of cation vacancies, V, in the cation sublattice of the binary oxide. Thus, the fluxes of cations and vacancies are coupled, $j_{A^{2+}} + j_{B^{2+}} + j_V = 0$ (see Fig. 1b). If both cations have different mobilities, the originally homogeneous oxide will become inhomogeneous, as depicted in Fig. 1b. The faster of the two components A and B becomes enriched at the high-p_{O_2} side, while the slower component is left behind and becomes enriched at the low-p_{O_2} side.

If the cations and cation vacancies arrive at the crystal surfaces chemical reactions have to take place. At the high-p_{O_2} side, cations A^{2+} (and B^{2+}), are oxidized by oxygen, O_2(g), from the gas phase, and cation vacancies, V, electron holes, $h^\bullet$, and new lattice molecules, AO (and BO), of the oxide are produced. At the low-p_{O_2} side the opposite reactions take place, i.e., cation vacancies and electron holes are annihilated, and oxide molecules are reduced to cations and oxygen.

$$A^{2+} + \frac{1}{2}O_2(\text{gas}) \underset{\text{reduction}}{\overset{\text{oxidation}}{\rightleftharpoons}} V + 2h^\bullet + AO \tag{1}$$

$$B^{2+} + \frac{1}{2}O_2(\text{gas}) \underset{\text{reduction}}{\overset{\text{oxidation}}{\rightleftharpoons}} V + 2h^\bullet + BO \tag{2}$$

As a consequence of these reactions, both oxide surfaces shift to the side of higher oxygen potential. In summary, the external oxygen potential gradient causes

- a directed flux of cation vacancies, $j_V = -j_{A^{2+}} - j_{B^{2+}}$, from the high to the low oxygen potential side of the oxide;
- a drift motion of both crystal surfaces towards the high-p_{O_2} side; and
- demixing of the cations with enrichment of the faster cation at the high-p_{O_2} side.

*Oxygen ion-conducting oxides will be considered later on.

**In most cases, the results obtained for binary oxides can easily be transferred to higher oxides.

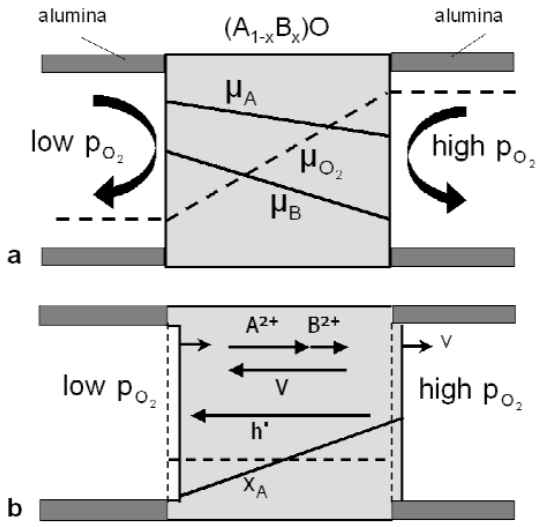

Fig. 1 Schematic experimental setup of an oxide that is exposed to an oxygen potential gradient (established, e.g., by different gas mixtures on both sides). (a) Chemical potential gradients of the chemical components A, B, and O. (b) Fluxes of cations, A^{2+} and B^{2+}, cation vacancies, V, and electron holes, $h^{\bullet}$, and demixing profile of the faster component A and shift of the crystal surfaces.

The demixing will start at the crystal surfaces, and after some time a steady state will be reached where both crystal surfaces move with the same, constant velocity and the demixing profile has become stationary (relative to the moving surfaces).

The phenomenon of kinetic demixing was first analyzed by Schmalzried et al. [7] and experimentally demonstrated using as a model system the oxide solid solution $(Co_{1-x}Mg_x)O$, where Co is the faster component. As expected, strong enrichment of Co was found at the high-p_{O_2} side of the material.

Formal treatment of demixing in an oxygen and electric potential gradient

In this section, the basic equations, which are necessary for the formal treatment of the demixing problem, will be given. In addition to the oxygen potential gradient, which was discussed qualitatively in the previous section, an additional electric potential gradient will be applied to the oxide. Since the basic equations for both forces are similar, both phenomena can be treated simultaneously. At first, the steady-state demixing problem will be solved, and then the transient demixing problem will be analyzed.

As known from linear, irreversible thermodynamics [8], the driving forces for the motion of charged species (index *i*) are the gradients of their electrochemical potentials, $\eta_i = \mu_i + z_i \cdot F \cdot \Phi$, where μ_i is the chemical potential, z_i the charge number, F Faraday's constant, and Φ the electric potential. The corresponding equations for cations, A^{z_A+} and B^{z_B+}, and electron holes, $h^{\bullet}$, are*

$$j(A^{z_A+}) = -L_{AA}\nabla\eta(A^{z_A+}) - L_{AB}\nabla\eta(B^{z_B+}) - L_{Ah}\nabla\eta(h^{\bullet}) \quad (3)$$

$$j(B^{z_B+}) = -L_{BA}\nabla\eta(A^{z_A+}) - L_{BB}\nabla\eta(B^{z_B+}) - L_{Bh}\nabla\eta(h^{\bullet}) \quad (4)$$

$$j(h^{\bullet}) = -L_{hA}\nabla\eta(A^{z_A+}) - L_{hB}\nabla\eta(B^{z_B+}) - L_{hh}\nabla\eta(h^{\bullet}) \quad (5)$$

*Here, we have permitted different charges, z_A and z_B for both cations.

The quantities L_{ij} are the Onsager transport coefficients [8].

Steady-state demixing

In the steady state, both cations are moving with the same velocity, v_{stat}, relative to the immobile oxygen sublattice of the oxide. Since the fluxes can always be written as a product of a velocity and a concentration, $j_i = v \cdot c_i$, the steady-state condition is given by:

$$v_{stat} = \frac{j(A^{z_A+})}{c_A} = \frac{j(B^{z_B+})}{c_B} \tag{6}$$

Inserting eqs. 3 and 4 into eq. 6, we obtain the "demixing equation", which relates the two forces on the chemical components A ($\leftrightarrow A^{z_A+} - z_A h^\bullet$) and B ($\leftrightarrow B^{z_B+} - z_B h^\bullet$), $\nabla\mu_A$ and $\nabla\mu_B$, and the force on the electron holes, $\nabla\eta(h^\bullet)$:

$$\nabla\mu_B = \Psi \cdot \nabla\mu_A + \Gamma \cdot \nabla\eta(h^\bullet) \tag{7}$$

The functions Ψ and Γ are given by

$$\Psi = \frac{x_B \cdot L_{AA} - x_A \cdot L_{BA}}{x_A \cdot L_{BB} - x_B \cdot L_{AB}}, \quad \Gamma = \frac{x_B \cdot z_A^{eff} \cdot L_{AA} - x_A \cdot z_B^{eff} \cdot L_{BB}}{x_A \cdot L_{BB} - x_B \cdot L_{AB}} \tag{8}$$

where z_A^{eff} and z_B^{eff} are the so-called effective charges of A and B:

$$z_A^{eff} = z_A + \frac{L_{Ah}}{L_{AA}} + z_B \frac{L_{AB}}{L_{AA}}, \quad z_B^{eff} = z_B + \frac{L_{Bh}}{L_{BB}} + z_A \frac{L_{AB}}{L_{BB}} \tag{9}$$

The effective charges contain the diagonal coefficients and the cross-coefficients of the Onsager transport matrix. The former describe the direct influence of the forces, while the latter express the flux coupling between different mobile components. For example, L_{AB} describes the flux of A^{z_A+} due to the force $\nabla\eta(B^{z_B+})$ (see eq. 3), and, because of the Onsager relation, $L_{AB} = L_{BA}$, also the opposite effect, i.e., the flux of B^{z_B+} owing to the force $\nabla\eta(A^{z_A+})$ (see eq. 4). This means that the difference between the effective charges, z_i^{eff}, and the formal charges, z_i, has a purely kinetic origin.

Steady-state demixing in an oxygen potential gradient

If only an external oxygen potential gradient, but no external electric potential gradient, is applied there will be no net electric current, i, through the oxide (ambipolar diffusion). Then, the gradient of the electrochemical potential of the electron holes in eq. 7, $\nabla\eta(h^\bullet)$, can be computed from the condition $i = 0$. Since the oxide under consideration is a good semiconductor, the transport coefficient of electron holes is much larger than all other transport coefficients, $L_{hh} >> L_{ij}$, and the corresponding force is approximately zero, $\nabla\eta(h^\bullet) \approx 0$. Thus, the demixing equation (7) simplifies to $\nabla\mu_B = \Psi\nabla\mu_A$, and only the parameter Ψ determines the demixing behavior. To proceed, we have to distinguish between nearly ideal, homovalent solid solutions of AO and BO and heterovalently doped oxides with strong deviations from ideality. In the former case, the Onsager cross-coefficients can be neglected in the expression for Ψ (see eq. 8), whereas in the latter case, the cross-coefficients have to be considered.

Homovalent, ideal solid solution of AO and BO

If the cross-coefficients are negligible, the diagonal coefficients are given by $L_{ii} = D_i c_i/RT$ (D_i and c_i are the diffusion coefficient and concentration of species i), and Ψ simplifies to $\Psi = D_A/D_B$. Then, the demixing equation takes the simple form

$$\nabla\mu_B = (D_A/D_B) \cdot \nabla\mu_A \tag{10}$$

Using the equilibria $A + \frac{1}{2}O_2(g) \leftrightarrow AO$ and $B + \frac{1}{2}O_2(g) \leftrightarrow BO$, and assuming an ideal solid solution of AO and BO, we obtain $\nabla\mu_A + 1/2\,\nabla\mu_{O_2} = \nabla\mu_{AO} = RT\,\nabla\ln x_A$ (x_A is the molar fraction of A)

and an analogous expression for B, $\nabla\mu_B + 1/2\,\nabla\mu_{O_2} = \nabla\mu_{BO} = RT\nabla\ln x_B$. With these relations, eq. 10 can be written as:

$$\left(\frac{1}{1-x_A}+\frac{D_A}{D_B}\cdot\frac{1}{x_A}\right)\cdot RT\nabla x_A = \left(\frac{D_A}{D_B}-1\right)\cdot\tfrac{1}{2}\nabla\mu_{O_2} \tag{11}$$

Equation 11 shows that the ratio D_A/D_B determines whether there is kinetic demixing and at which side of the oxide component A becomes enriched. If both components have the same diffusion coefficient, $D_A/D_B = 1$, there will be no demixing, $\nabla x_A = 0$. If $D_A/D_B > 1$ (A is the faster component), ∇x_A has the same sign as the oxygen potential gradient, $\nabla\mu_{O_2}$, i.e., A becomes enriched at the high-p_{O_2} side. If, on the other hand, B is the faster component, $D_A/D_B < 1$, A becomes enriched at the low-p_{O_2} side. As shown by Schmalzried et al. [7], the demixing profile is then obtained by integration of eq. 11 with appropriate boundary conditions. The resulting theoretical demixing profiles are in good agreement with the experimentally found demixing profiles.

Heterovalently doped oxide

If the oxide AO is heterovalently doped (e.g., with an oxide B_2O_3), the excess charge of the dopant ion B^{3+} (compared to the host ion A^{2+}) results in the formation of charge-compensating cation vacancies, V. Then the oxide solid solution, $(A_{1-x}B_x)O$, can no longer be treated as an ideal solution. As shown in detail in ref. [9], in a dilute oxide, $A_{1-x}B_xO$ ($x << 1$), the flux of the dopant, B, can be written as:

$$j_B = -D_B\cdot\nabla c_B - j_V\cdot\frac{L_{BB}}{L_{AA}}\cdot\left(\rho+\frac{L_{BA}}{L_{BB}}\right) \tag{12}$$

The dimensionless quantity ρ contains all physical correlation effects and is of the order of 1. Equation 12 shows that the dopant flux consists of two terms, a pure diffusion term, $-D_B\nabla c_B$, characterized by the dopant diffusion coefficient, D_B ($=L_{BB}RT/c_B$), and a drift term, that is proportional to the directed vacancy flux, j_V. The direction of the drift term, which determines on which side of the sample the dopant becomes enriched, depends crucially on the sign and magnitude of the nondiagonal element L_{BA}. In heterovalently doped oxides, e.g., $AO(+B_2O_3)$, solute-vacancy interactions might result in a nonvanishing and negative cross term L_{AB}. These interactions are caused by the coulombic interaction between the excess charges of the defects.*

The interaction of the dopant ion with its neighbors may be weak (as is expected for homovalent dopant ions) or stronger (for heterovalent dopant ions). If the interaction is weak, dopant ions and vacancies do not form bound pairs but drift in opposite directions. For strong attractive interaction, on the other hand, dopant ions and vacancies form bound pairs, and the dopant ions drift in the same direction as the vacancies.

This qualitative picture is confirmed by a microscopic diffusion model that considers nearest-neighbor interactions. The so-called five-frequency model [10] uses five exchange frequencies of vacancies and ions (see Fig. 2): ω_0 and ω_1 for exchange of vacancies with solvent ions in the pure crystal (i.e., far away from the solute ion) and in the nearest neighborhood of the solute ion; ω_3 for vacancy jumps, which dissociate a solute-vacancy pair; ω_4, which creates a new pair; and ω_2 for exchange of a vacancy and a solute ion. ω_3 and ω_4 are coupled by the condition of detailed balance, $\omega_4/\omega_3 = \exp(-\Delta g_{pair}/RT)$, where Δg_{pair} is the binding Gibbs energy of the solute-vacancy pair.

*Cation vacancies possess a negative excess charge relative to the ideal lattice, while, e.g., trivalent dopant ions possess a positive excess charge. This is more evident using the Kröger–Vink notation for the vacancy, V_A'', and the dopant ion, $B_A^\bullet$ (prime and dot indicate negative and positive excess charges, respectively).

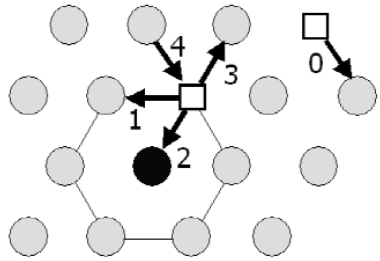

Fig. 2 Five-frequency model of solute diffusion (● = solvent cation, ● = solute cation, □ = cation vacancy). ω_k (k = 0,1,2,3,4) = exchange frequencies of vacancies and cations (see text).

Within this model, the transport coefficients L_{ij} (i,j = A,B) are known exactly [10]

$$L_{AA} = \lambda_{AA}^{free}(\omega_0)\cdot x_V^{free} + \lambda_{AA}^{pair}(\omega_k)\cdot x_p \tag{13}$$

$$L_{AB} = \lambda_{AB}(\omega_k)\cdot x_p,\quad L_{BB} = \lambda_{BB}(\omega_k)\cdot x_p \tag{14}$$

The index "free" denotes ionic motion by means of free (i.e., unbound vacancies with molar fraction x_V^{free}), while the index "pair" denotes ionic motion by means of vacancies that are bound in solute-vacancy pairs (molar fraction x_p). The functions $\lambda_{ij}(\omega_k)$ are known functions of the five exchange frequencies ω_k (k = 0,1,2,3,4) [10]. Whereas λ_{AA} and λ_{BB} are always positive, λ_{AB} becomes negative for strong, attractive solute-vacancy interaction. As a consequence of eq. 14, the ratio L_{AB}/L_{BB} in eq. 12 is a constant, $L_{AB}/L_{BB} = \lambda_{AB}/\lambda_{BB}$, which depends only on the exchange frequencies, ω_k, and not on the fractions of free or bound vacancies. Thus, the direction of the solute drift flux is only determined by the solute-vacancy binding energy [9].

Demixing experiments with Ga_2O_3-doped CoO [11] clearly show demixing of Co and Ga with enrichment of Ga at the low oxygen potential side (see Fig. 3). Since the tracer diffusion coefficients of Co and Ga are also known [12], the ratio L_{GaCo}/L_{GaGa} can be obtained from the demixing profile using eq. 14. The result is $L_{CoGa}/L_{GaGa} = -1.7$, leading to the following interpretation. Owing to strong binding between the dopant Ga and the vacancies, solute-vacancy pairs, $\{Ga^{3+},V\}(\equiv\{Ga_{Co}^{\bullet}, V_{Co}''\}')$ are formed, and the drift flux of the dopant is directed to the side of lower oxygen potential (i.e., in the same direction as the vacancy flux), where the dopant Ga therefore becomes enriched (see Fig. 3).

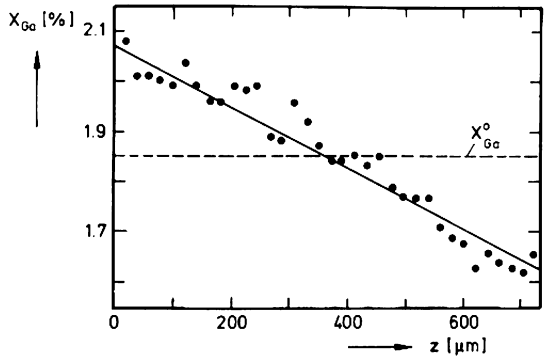

Fig. 3 Demixing profile of Ga in $(Co_{1-x}Ga_x)O$ exposed to an oxygen potential gradient (T = 1250 °C, $p_{O_2}^{(1)} = 10^{-6}$ bar (left), $p_{O_2}^{(2)} = 10^{-5}$ bar (right), Δz = 725 µm, x_{Ga}^0 = 1.85 %, t = 38.5 h) [11].

Steady-state demixing in an oxygen ion conductor

Demixing in an oxygen potential gradient might be important also in oxygen ion conductors, such as yttria-doped zirconia (YSZ) or SrO- and MgO-doped lanthanum gallate (LSGM). When these oxides are used as electrolytes, e.g., in solid oxide fuel cells (SOFCs), oxygen ions are driven through the electrolyte and simultaneously electrons are flowing through the external circuit. As soon as the cations, e.g., Zr^{4+} and Y^{3+} in YSZ, have different diffusion coefficients, there will be demixing of the electrolyte. The detailed formal analysis can be found in refs. [13,14]. Since cation diffusion is very slow in these oxides [15,16], steady-state demixing will be reached only after rather long times. If, for example, the slowest diffusion coefficient is taken as $D = 10^{-14}$ cm^2 s^{-1}, one obtains 15 000 years for an electrolyte thickness of 1 mm. However, for a thickness of 10 μm (which is the target for future SOFCs), the time to reach the steady state is only 1.5 years, which is comparable to the desired operating times of SOFCs.

Steady-state demixing in a pure electrical potential gradient

Bray and Merten [17] were the first to raise the possibility of demixing occurring in a solid electrolyte due to an electrical field. Monceau et al. [18] performed a quantitative formulation of the kinetic demixing problem in an electrical potential gradient and presented the results of demixing experiments for a (Co,Mg)O solid solution. Systematic theoretical and experimental studies of demixing of homovalent oxide solid solutions and heterovalently doped oxides in an electric potential gradient were performed by Teller and Martin [19–21].

Homovalent, ideal solid solution of AO and BO

The electrical potential gradient causes fluxes of the cations, A^{2+} and B^{2+}, and the electron holes, $h^{\bullet}$, which are given by eqs. 3–5. To apply the electric potential gradient, inert electrodes (e.g., Pt-electrodes) are used which are the source or sink of electrons. For example, at the cathode the following reactions take place:

$$A^{2+} + 2e^{-}(Pt) + \tfrac{1}{2}O_2(g) \rightarrow V + AO, \quad B^{2+} + 2e^{-}(Pt) + \tfrac{1}{2}O_2(g) \rightarrow V + BO \tag{15}$$

This means that the oxide grows at the cathode. At the anode the opposite reactions take place, i.e., here the oxide dissociates into cations, electrons and oxygen molecules. Thus, both oxide surfaces move to the cathode side. In the steady state both surfaces and also both cations move with the same velocity (see eq. 6), as in the case of a pure oxygen potential gradient. However, now the term $\nabla\eta(h^{\bullet})$ cannot be neglected in eq. 7. Rearrangement of eq. 7 yields:

$$\frac{\gamma - x_A}{x_A \cdot (1 - x_A)} \cdot \nabla x_A = -\frac{2}{RT} \cdot \nabla \eta_{h^{\bullet}} \tag{16}$$

After integration of eq. 16 over the overall sample thickness one obtains with $\nabla\eta_{h^{\bullet}} = U \cdot F$ (U is the applied voltage):

$$\frac{x_A^{(1)}}{x_A^{(2)}} \cdot \frac{1 - x_A^{(2)}}{1 - x_A^{(1)}} = \exp\left(\frac{2 \cdot F \cdot U}{R \cdot T} \cdot \frac{\gamma - 1}{\gamma}\right) \tag{17}$$

where $x_A^{(1)}$ and $x_A^{(2)}$ are the unknown molar fractions of A at the oxide surfaces. $\gamma = D_A/(D_A - D_B)$ is a constant, since both diffusion coefficients are proportional to the cation vacancy fraction, x_V. The concentration profile of A (and B, $x_A + x_B = 1$) can be obtained by integration of eq. 16 and the overall mass balance for A. Details can be found in [19]. Figure 4 shows steady-state demixing profiles calculated in this way for different values of the applied voltage U. With increasing voltage, the anode-side of the oxide is more and more depleted by the faster component A.

A typical result of a steady-state demixing experiment for $(Co_{1-x}Ni_x)O$ is shown in Fig. 5. Enrichment of Co near the cathode side of the oxide is found [14,21], as expected qualitatively due to

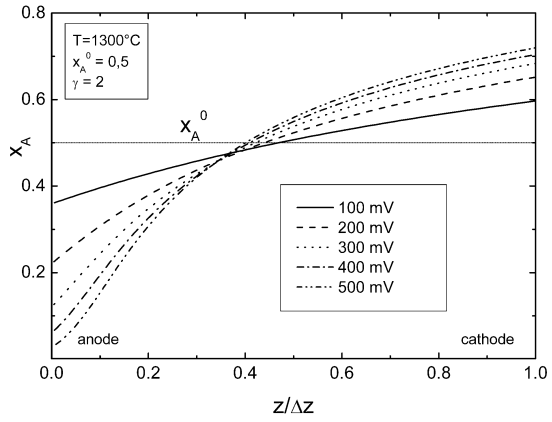

Fig. 4 Dependence of the steady-state demixing profile of component A in (A,B)O on the applied voltage U (T = 1300 °C, $x_A^0 = 0.5$, $\gamma = D_A/(D_A - D_B) = 2$, $z = 0$: anode, $z = \Delta z$: cathode).

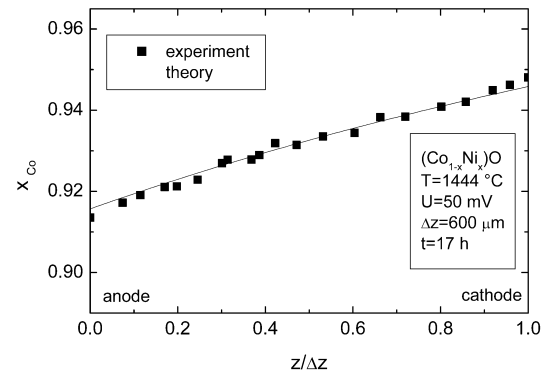

Fig. 5 Steady-state demixing profile of Co in $(Co_{1-x}Ni_x)O$ (T = 1444 °C, U = 50 mV, $x_A^0 = 0.932$, Δz = 600 μm, t = 17 h).

the higher diffusivity of Co compared to Ni [22]. However, a quantitative modeling of the demixing profile (solid line in Fig. 5) is only possible if the effective charges (see eq. 9) of Co and Ni are chosen as $z_{Co}^{eff} \approx 1$ and $z_{Ni}^{eff} \approx 1$. The strong deviation from the formal charges, $z_{Co} = 2$ and $z_{Ni} = 2$, is due to the fact that the cross-terms L_{Coh} and L_{Nih} are by no means negligible and negative, $L_{Coh}/L_{CoCo} \approx -1$ and $L_{Nih}/L_{NiNi} \approx -1$. A similar result was found during tracer drift experiments in pure CoO exposed to an electric field and explained by association between cation vacancies and electron holes [23]. Finally, it should be emphasized that the electric current during demixing is mainly conducted by electron holes, because $t_h \cong 1$ and $t_{cation} << 1$. Nevertheless, there is a demixing process for the cations as long as they have different mobilities.

Heterovalently doped oxide

Demixing in a heterovalently doped oxide, e.g., $AO(+B_2O_3)$, is more complicated. Owing to coulombic interactions between the defects (solute-vacancy pairs), the cross term L_{AB} can no longer be neglected and might determine the complete demixing behavior (as in the case of an applied oxygen potential gradient). An example is again Ga-doped CoO, $(Co_{1-x}Ga_x)O$, in which Ga-ions, $Ga_{Co}^{\bullet}$, and cation vacancies, V_{Co}'', (Kröger–Vink notation) form solute-vacancy pairs, $\{Ga_{Co}^{\bullet}, V_{Co}''\}'$. These pairs have a negative excess charge and are driven by the electric potential gradient towards the anode. Thus, Ga is enriched at the anode side, independent of the ratio of the diffusion coefficients of Co and Ga [20].

Transient demixing

To obtain the transient demixing behavior prior to the steady state, the transport equations (eqs. 3–5) with the appropriate boundary conditions were solved numerically (nonlinear diffusion problem with moving boundaries and time-dependent boundary conditions). Demixing of homovalent, ideal oxide solid solutions in an oxygen potential gradient [24] and in an electric potential gradient [25] was analyzed. Here, only the former case will be discussed.

The results on the time evolution of the demixing profiles, $x_A(z,t)$ in (A,B)O exposed to an oxygen potential gradient are shown in Fig. 6a [the numerical calculations were performed with a parameter set for the oxide solid solution (Co,Mg)O]. It can be seen that after about 20 days the steady state is reached. The analytically computed, stationary demixing profile (represented by open circles in Fig. 6a) agrees well with the numerical solution. The results on the temporal variations of the vacancy fraction, $x_V(z,t)$, during demixing are illustrated in Fig. 6b. It should be noted that x_A and x_V at the boundaries continuously change with time until the steady state is reached.

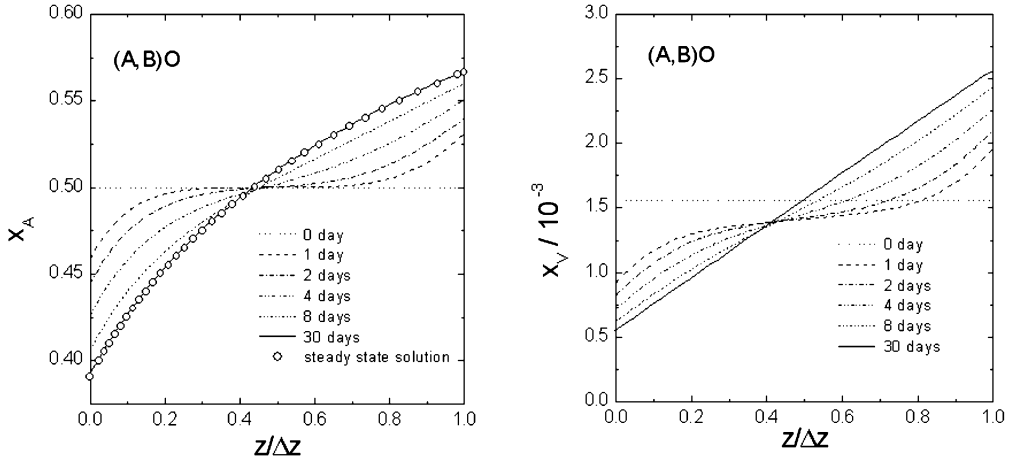

Fig. 6 (a) Temporal variations of the spatial distribution of x_A in (A,B)O. The steady-state demixing profile computed analytically is represented by open circles. (b) Temporal variations of the spatial distribution of the vacancy fraction, x_V [24].

Figure 7a shows the time dependence of the boundary velocities, v^I and v^{II} (low- and high-oxygen potential side, respectively). Both velocities decrease with time and eventually approach a constant value that corresponds to the steady-state velocity, v^{st}. Considering the time dependencies of $x_V(z,t)$ and the surface velocities, v^I and v^{II}, two transient processes are involved in the demixing process.

The first transient process corresponds to the establishment of a quasi-stationary distribution of $x_V(z,t)$ (see Fig. 7b), and both surface velocities show a fast rate of change (see insert in Fig. 7a). However, the degree of demixing is negligible during this time period (see Fig. 7b). The typical relaxation time, τ_1, for this process is determined by chemical diffusion of the vacancies in the oxide solid solution having an approximately homogeneous composition. The estimated time, $\tau_1 = 20$ min, agrees well with the numerically obtained relaxation time [24].

The second transient process with a relaxation time τ_2 can be characterized by the evolution of the demixing profile, $x_A(z,t)$, across the oxide. Because these compositional changes demand cationic motion, τ_2 can be estimated from the mean-square displacement of the cations, $\tau_2 = (\Delta z)^2/(2\bar{D}_{cation})$, where Δz is the crystal thickness and $\bar{D}_{cation}$ the average cation self-diffusion coefficient. The estimated value for τ_2 is ca. 490 h. It compares well with the numerically obtained value of about 480 h. It should be noted that $x_V(z,t)$ also shows temporal variations during the second relaxation process, however, at a slow rate, which confirms the previous assumption of a quasi-steady state.

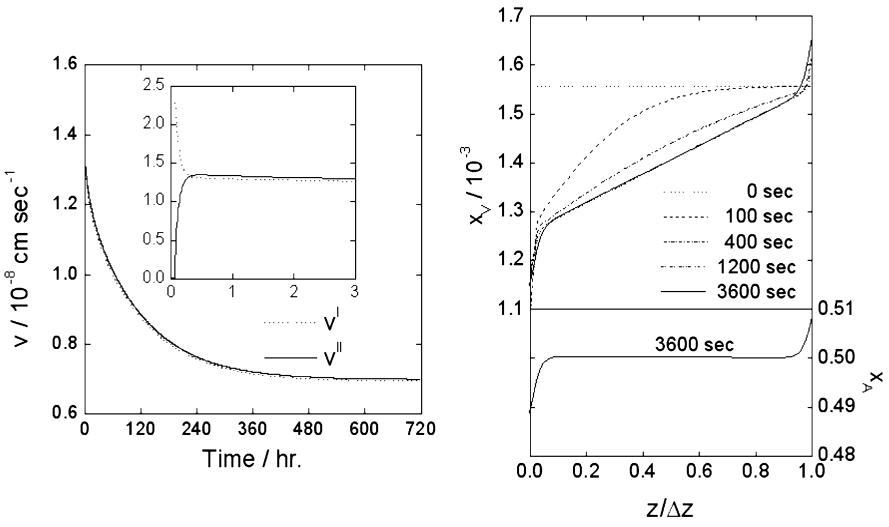

Fig. 7 (a) Temporal variations of the boundary velocities v^{I} and v^{II} during the demixing process. The changes during the first 3 h are shown in the inset. (b) Temporal variations of the spatial distribution of x_V (upper part) and x_A (lower part) during the first hour [24].

Kinetic decomposition

If during demixing due to an external thermodynamic force, the stability field of the material is left, decomposition of the material and the formation of new phases might take place (kinetic decomposition). First, Schmalzried and Laqua [26] observed the formation of a multiphase layer in the system NiO–TiO_2 after exposure of a single-phase $NiTiO_3$-crystal to an oxygen potential gradient. While (Ni,Ti)O is formed at the high-oxygen potential side, TiO_2 was found at the low-oxygen potential side of the crystal. The origin of this process is again the difference of the diffusion coefficients of Ni and Ti in $NiTiO_3$, but now demixing is driven to the point where the stability field of the oxide is left. Kinetic decomposition was also found for fayalite, Fe_2SiO_4, exposed to an oxygen potential gradient [27] (formation of SiO_2 and Fe_3O_4 at the low-, respectively, high-oxygen potential side) and for the system NiO–SiO_2 in an oxygen potential gradient [28,29].

MORPHOLOGICAL INSTABILITIES

During a diffusion-controlled solid-state reaction, matter is transported toward (or away from) an interface that separates the reactants and the product. The progress of the reaction is strongly determined by the morphology of the interface, because the morphology determines the boundary conditions for the transport problem. One-dimensional diffusion with a planar interface is only a special case, since often morphological instabilities result in nonplanar interfaces with complicated structures, which can roughly be classified as cellular, dendritic, or fractal. The morphological stability of interfaces belongs to the wide class of self-organization or pattern-formation problems arising in biology, physics, chemistry, and geology, in which a nonequilibrium system forms new structures. Examples are complex biological systems, dendrites during the growth of snowflakes, the Bénard-instability or spatio-temporal structures during the formation of the so-called Liesegang rings [30,31]. In all these different systems, new structures develop through instabilities from stationary structures as a result of changed external parameters (control parameters).

In the next two sections, we will review two types of solid-state reactions where we have found complicated morphological instabilities, which may serve as model reactions. Our first example is a

solid/solid interface between two ionic conductors, which is driven by an applied electric field, and our second example concerns interdiffusion of ionic conductors in an electric field.

Morphology of an interface between two ionic conductors

To study the morphology of an interface between two crystalline solids, we consider a diffusion couple consisting of two ionic conductors and apply an external electric field as the driving force for the motion of the solid/solid interface. To focus on the essential part of the problem, we study a phase boundary between two immiscible ionic conductors. In the experiments, we use the quasi-binary system AgCl–KCl as a model system. Below the eutectic temperature, T_e = 306 °C, there is no mutual solubility, although AgCl as well as KCl crystallize in the rock-salt structure. However, the lattice constants of both compounds are very different, resulting in a mismatch of about 12 %. Both compounds are practically pure cation conductors. In AgCl (cation Frenkel disorder), silver-ions are mobile in the interstitial sublattice, while in KCl (Schottky disorder), potassium-ions are mobile by means of cation vacancies. As a result of the different disorder types, the ionic conductivity in AgCl is about 6 orders of magnitude larger than in KCl. Experiments were done with AgCl- and KCl-single crystals, which were used in an electrochemical cell +/Ag/AgCl/KCl/Ag/– [32]. Silver-ions, Ag^+, are driven by the applied electric potential difference from the Ag-anode to the boundary AgCl/KCl. Since Ag is not soluble in KCl, the following exchange reaction takes place:

$$Ag^+ + KCl \rightarrow AgCl + K^+ \tag{18}$$

This exchange reaction has two consequences: (i) it allows further charge transport by means of K^+-ions, and (ii) the AgCl-phase grows at the expense of the KCl-phase. Since transport in AgCl is much faster than in KCl, the applied electric potential falls off across the "slower" KCl crystal. Again, this has two consequences: (i) the interface is an isopotential line, and (ii) the rate-determining step for the motion of the interface between the two solids is the flux of K^+-ions in KCl (or the oppositely directed flux of the cation vacancies). Therefore, any spatial perturbation of the plane interface will grow faster than the plane interface itself (the electric field at the tip of the perturbation is larger than at the plane interface). From this simple argument, and by analogy with previous experiments at gas/oxide interfaces [33–35], we expect the planar solid/solid phase boundary between AgCl and KCl to be morphologically unstable, if we apply the potential difference in such a way that AgCl grows. If we reverse the applied voltage, we expect the boundary to be stable. This picture is confirmed by the results of a linear stability analysis [32] for the moving solid/solid interface. A typical experimental result, demonstrating that the solid/solid interface is morphologically unstable is shown in Fig. 8. We note that AgCl

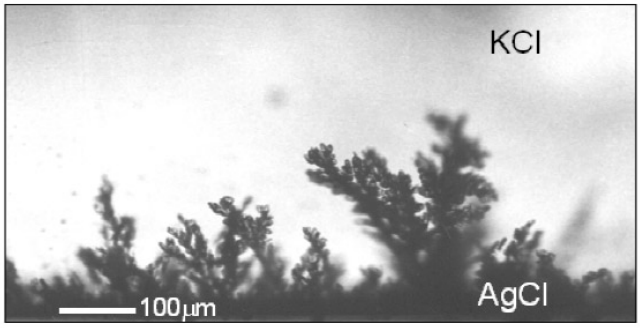

Fig. 8 Cross-section of the unstable solid/solid interface between AgCl (dark) and KCl (bright) in an electric potential gradient. (T = 563 K, t = 42 h, electric field = 10 V/mm, bottom: anode, top: cathode). The micrograph was taken in an optical microscope [32].

grows into KCl in the form of "trees", which are typical of fractal growth phenomena [36]. Closer inspection shows that these trees are 2D objects, with certain orientations in the KCl-matrix, which are probably the result of elastic effects due to the different lattice constants of both materials. If the polarization of the cell is reversed, i.e., –Ag/AgCl/KCl/Ag/+, the plane interface between AgCl and KCl is morphologically stable as expected. A more detailed discussion can be found in ref. [32].

Similar morphologies as observed in the experiments can be produced in Monte Carlo simulations [37,38]. In these simulations, we start from an atomistically flat interface between two ionic conductors AX (black) and BX (white) (see Fig. 9). A vacancy is introduced at the top of the simulation lattice and exchanges sites with ions A and B. These ions interact by means of short range interactions ε_{AA}, ε_{BB} and ε_{AB}, and, therefore, the vacancy (i) performs a correlated random walk, and (ii) causes a motion of the interface between the two ionic conductors. An external electric field causes an additional drift motion of the vacancy. When the vacancy reaches the bottom of the simulation lattice, it is killed. With this simple model, a variety of interface morphologies can be produced [38].

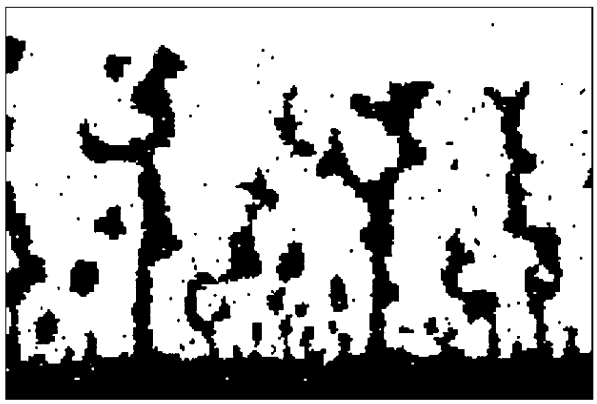

Fig. 9 Monte Carlo simulation of the interface between two ion conductors in an electric field (black: good ionic conductor, white: bad ionic conductor, bottom: anode, top: cathode) [38].

If the simulation is performed in the same way as the previously described experiment, i.e., the faster phase (black) grows at the expense of the slower phase (white), the interface is morphologically unstable. The simulated morphology in Fig. 9 is qualitatively in agreement with the experimentally observed one in Fig. 8. If the direction of the vacancy flux during the Monte Carlo simulation is reversed (corresponding to a change of the polarization in the experiment), the plane surface is morphologically stable, as observed experimentally.

Instability of diffusion fronts in electric fields

In the previous section, we have demonstrated that the moving interface between two immiscible ionic conductors, which is driven by an external electric field, is morphologically unstable when the "faster" of both phases grows. In this chapter, we will analyze what happens if we go to the other extreme (i.e., if the two ionic conductors are totally miscible). A good example is provided by the system AgCl–NaCl. Between the critical temperature T_c = 198 °C (below which there is a miscibility gap with mutual solubilities) and the melting temperature of AgCl, both compounds form a complete solid solution. As before, Ag^+-ions in AgCl are mobile in the interstitial sublattice, Na^+-ions in NaCl are mobile by means of cation vacancies, and the ionic conductivity, σ, in AgCl is orders of magnitude larger than in NaCl. In the solid solution, $(Ag_{1-x}Na_x)Cl$, σ decreases exponentially with the composition x [39]. Experiments were performed in the same way as before with an electrochemical cell

+/Ag/AgCl/NaCl/Ag/– [40]. However, in contrast to the previous experiment, we have now a combination of two effects, interdiffusion of Ag^+ and Na^+, and drift in the externally applied electric potential gradient. Since the diffusion coefficients of Ag^+ and Na^+ depend exponentially on composition, x, pure interdiffusion would result in very steep interdiffusion profiles. If we apply in addition an electric field in such a way that the faster "phase" (in this case, the Ag-rich part of the solid solution) grows, we expect morphological instabilities, in analogy to the previously discussed case and according to the principle formulated there. It has to be emphasized, however, that these expected morphological instabilities are instabilities of diffusion fronts in a single-phase system without any phase boundary.

Figure 10 shows a typical result of an interdiffusion and drift experiment. The picture was obtained in an electron microscope using back-scattered electrons, which indicate a phase contrast. In the picture, the steep concentration gradient in the interdiffusion zone appears as sharp phase contrast, but microprobe analysis confirms a steep concentration gradient in a single-phase system.

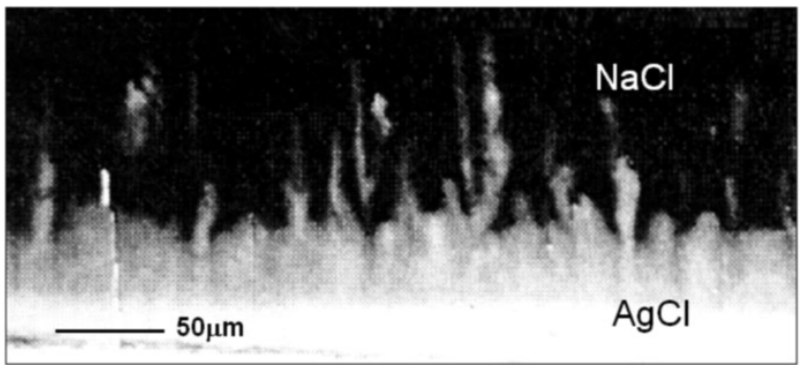

Fig. 10 Cross-section of the interdiffusion zone between AgCl (bright) and NaCl (dark) in an electric field (T = 523 K, t = 14 h, electric field = 720 V/mm, bottom: anode, top: cathode). The micrograph was taken in a scanning electron microscope [40].

While the interdiffusion profile without an external electric field is one-dimensional (i.e. planar as expected), it is by no means one-dimensional with an applied electric field. Instead, one can observe instabilities of the diffusion fronts in the form of "fingers".

CONCLUSIONS

We have discussed three types of degradation mechanisms for materials in thermodynamic potential gradients, kinetic demixing, kinetic decomposition, and morphological instabilities, all of which are of great significance for the application of materials. For the cation demixing in a solid solution of homovalent oxides, $(A_{1-x}B_x)O$, we have reviewed the formal analysis of the transport problem. As expected, the faster cation is enriched at the cathode. Experiments were performed with the model system $(Co_{1-x}Ni_x)O$, confirming the theoretical results. In contrast, the demixing behaviour in heterovalently doped oxides, such as $(Co_{1-x}Ga_x)O$, is determined by the formation of dopant-vacancy pairs. As a result of this interaction, the cross term L_{CoGa} can no longer be neglected and dominates the demixing behaviour, independent of the ratio of the diffusion coefficients of both cations.

For diffusion-controlled solid-state reactions in an external electric field, we have found morphological instabilities of an originally planar solid/solid interface and of diffusion fronts. Experiments have been performed with diffusion couples of two ionic conductors. The interface AgCl/KCl exhibits fractal-like morphological instabilities, while the diffusion fronts in the totally miscible system AgCl–NaCl exhibit finger-like instabilities. With these experimental results, we may formulate the fol-

lowing simple principle for the stability of a moving interface during a solid-state reaction. A moving interface between two phases is morphologically unstable if the "faster" phase (i.e., the phase with the higher mobility) grows, while it is morphologically stable if the "slower" phase grows. The two solid-state reactions discussed above confirm this simple principle.

REFERENCES

1. H. J. Grabke and M. Schütze (Eds.). *Oxidation of Intermetallics*, Wiley-VCH, Weinheim (1997).
2. U. Koops, D. Hesse, M. Martin. *J. Mater. Res*. **17**, 2489 (2002).
3. E. Ryshkewitch and D. W. Richerson. *Oxide Ceramics*, Academic, Orlando (1985).
4. A. Hammou and J. Guindet. In *The CRC Handbook of Solid State Electrochemistry*, P. J. Gellings and H. J. M. Bouwmeester (Eds.), pp. 407–443, CRC Press, Boca Raton (1996).
5. H. J. M. Bouwmeester and A. J. Burggraaf. In *The CRC Handbook of Solid State Electrochemistry*, P. J. Gellings and H. J. M. Bouwmeester (Eds.), pp. 481–553, CRC Press, Boca Raton (1996).
6. A. L. Laskar. In *Diffusion in Materials*, A. L. Laskar, J. L. Bocquet, G. Brebec, C. Monty (Eds.), NATO ASI Series E: Applied Sciences, Vol. 179, pp. 459–469, Kluwer, Dordrecht (1990).
7. H. Schmalzried, W. Laqua, P. L. Lin. *Z. Naturforsch*. **34a**, 192 (1979).
8. S. R. de Groot and P. Mazur. *Non-Equilibrium Thermodynamics*, North-Holland, Amsterdam (1962).
9. M. Martin. *Mater. Sci. Rep.* **7**, 1 (1991).
10. A. R. Allnatt and A. B. Lidiard. *Atomic Transport in Solids*, Cambridge University Press, Cambridge (1993).
11. M. Martin and R. Schmackpfeffer. *Solid State Ionics* **72**, 67 (1994).
12. R. Schmackpfeffer and M. Martin. *Phil. Mag*. *A* **68**, 747 (1993).
13. M. Martin. In *SOFC-VI*, S. C. Singhal (Ed.), PV 1999-19, pp. 308–316, Electrochemical Society Proceedings Series, Pennington, NJ (1999).
14. M. Martin. *Solid State Ionics* **136–137**, 331 (2000).
15. M. Kilo, G. Borchardt, B. Lesage, S. Weber, S. Scherrer, M. Martin, M. Schroeder. In *SOFC-VII*, H. Yokokawa and S. C. Singhal (Eds.), PV 2001-16, pp. 275–283, Electrochemical Society Proceedings Series, Pennington, NJ (2001).
16. O. Schulz, M. Martin, C. Argirusis, G. Borchardt. *Phys. Chem. Chem. Phys*. **5**, 2308 (2003).
17. D. T. Bray and U. Merten. *J. Electrochem. Soc.* **111**, 447 (1964).
18. D. Monceau, M. Filal, M. Tebtoub, C. Petot, G. Petot-Ervas. *Solid State Ionics* **73**, 21 (1994).
19. O. Teller and M. Martin. *Solid State Ionics* **101–103**, 475 (1997).
20. O. Teller and M. Martin. *Ber. Bunsen-Ges Phys. Chem.* **101**, 1377 (1997).
21. O. Teller and M. Martin. *Electrochemistry* **68**, 294 (2000).
22. W. K. Chen and N. L. Peterson. *J. Phys. Chem. Solids* **34**, 1093 (1973).
23. M. Martin and H.-I. Yoo. *Radiat. Eff. Defects Solids* **119–121**, 735 (1991).
24. J.-O. Hong, O. Teller, M. Martin, H.-I. Yoo. *Solid State Ionics* **123**, 75 (1999).
25. J.-O. Hong, H.-I. Yoo, O. Teller, M. Martin, J. Mizusaki. *Solid State Ionics* **144**, 241 (2001).
26. H. Schmalzried and W. Laqua. *Oxid. Metals* **15**, 339 (1981).
27. U. Brinkmann and W. Laqua. *Phys. Chem. Miner.* **12**, 283 (1985).
28. J. Wolfenstine, D. Dimos. D. L. Kohlstedt. *J. Am. Ceram. Soc*. **68**, 117 (1985).
29. K. T. Jacob and A. K. Shukla. *J. Mater. Res*. **2**, 338 (1987).
30. J. S. Langer. *Rev. Mod. Phys.* **52**, 1 (1980).
31. H. E. Stanley and N. Ostrowsky (Eds.). *On Growth and Form*, Martinus Nijhoff, Boston (1986).
32. S. Schimschal-Thölke, H. Schmalzried, M. Martin. *Ber. Bunsen-Ges. Phys. Chem*. **99**, 1 (1995).
33. M. Martin and H. Schmalzried. *Ber. Bunsen-Ges. Phys. Chem*. **89**, 124 (1984).
34. M. Martin. *Mater. Sci. Forum* **155–156**, 429 (1994).

35. M. Martin, P. Tigelmann, S. Schimschal-Thölke, G. Schulz. *Solid State Ionics* **75**, 219 (1995).
36. P. Meakin. *Phys. Rev*. *A* **27**, 2616 (1983).
37. G. Schulz and M. Martin. *Solid State Ionics* **101–103**, 417 (1997).
38. G. Schulz and M. Martin. *Faraday Discuss.* **106**, 291 (1997).
39. M. Matsushita, M. Sano, Y. Hayakawa, H. Honjo, Y. Sawada. *Phys. Rev. Lett.* **53**, 286 (1984).
40. S. Schimschal-Thölke, H. Schmalzried, M. Martin. *Ber. Bunsen-Ges. Phys. Chem*. **99**, 7 (1995).